Vailable online at www.sciencedirect.com

SciVerse ScienceDirect

Energy Procedia 27 (2012) 293 – 299

Energy Procedia

SiliconPV: April 03-05, 2012, Leuven, Belgium

Evaluating The Quality Of Selective Emitter Structures By Imaging The Emitter Saturation Current Density

M. Müller[a*], P.P. Altermatt[b], K. Schlegel[a], G. Fischer[a]

[a]*SolarWorld Innovations GmbH, Berthelsdorferstr. 111A, 09599 Freiberg, Germany*
[b]*Dep. Solar Energy, Inst. Solid-State Physics, Leibniz University of Hannover, Appelstr. 2, 30167 Hannover, Germany*

Abstract

A method to derive the emitter saturation current density J_{0e} with lateral resolution is applied to investigate selective emitter structures. The method uses PL lifetime imaging at several injection densities to laterally evaluate J_{0e} by applying the method of Kane and Swanson [1] pixel by pixel. Samples with two-sided diffused emitters on lowly-doped Cz wafers were used to produce selective emitter structures by laser doping of the phosphorus-rich glass (LDSE). By comparison of experimental and numerical simulation results of J_{0e} linescans, a limited resolution of a feature size of an inhomogeneous emitter is determined to be theoretically between 0.5-1.0 mm and experimentally about 2 mm. The method was successfully applied to investigate the dependence of J_{0e} on the laser power of a selective emitter structure. The expected behaviour of a maximum J_{0e} for medium laser intensities is observed. The method is suitable to evaluate the selective emitter process and its optimization.

Keywords: Emitter saturation current density; photoluminescence; selective emitter

1. Introduction

For the electrical characterization of silicon solar cells, it is common to quantify the saturation current density of the emitter J_{0e}. In this paper, we investigate selective emitters for crystalline Si solar cells, meaning that the emitter is highly-doped at the front metal contacts and rather lowly doped elsewhere. By now, it has been common to measure the J_{0e} of homogeneous samples, using the procedure of Kane and

* Corresponding author. Tel: +49-3731-301-1439; fax: +49-3731-301-1690
E-mail address: matthias.mueller@sw-innovations.de

1876-6102
doi:10.1016/j.egypro.2012.07.066

Swanson [1] in combination with the quasi-steady state photoconductance (QSSPC) method [2]. In this paper, we apply our recently developed imaging method for measuring J_{0e} with lateral resolution of inhomogeneous samples such as selective emitters [3]. We use photoluminescence (PL) measurements combined with photoconductance measurements to derive calibrated images of the effective excess carrier lifetime. At least two images under two different high-injection conditions are taken. The J_{0e} image is then derived, applying the method of Kane and Swanson [1] for each pixel. As an application of the method, the J_{0e} dependence on laser-doping with different laser intensities is shown.

2. Experimental method

In the method of Kane and Swanson [1], the effective lifetime of excess carriers τ_{eff} is measured as a function of the injection density Δn on a lightly doped wafer. The wafer is optimally [4,5] in high-level injection conditions because the recombination rate in the emitter is proportional to the square of Δn, and this recombination rate can then be separated from the linear recombination rate in the wafer. The inverse τ_{eff} can be expressed as [1]:

$$\frac{1}{\tau_{eff}} - \frac{1}{\tau_{Au}} = \frac{1}{\tau_{SRH}} + \left(J_{0e(front)} + J_{0e(back)} \right) \frac{(N_{dop} + \Delta n)}{qn_i^2 W}, \tag{1}$$

where N_{dop} is the wafer doping density, n_i is the intrinsic carrier density, q is the elementary charge, and W is the wafer thickness. τ_{Au} may be calculated from [6]. It is not necessary to know the Shockley-Read-Hall lifetime τ_{SRH} as long as it is not strongly injection-dependent, because to determine J_{0e} only the slope of $(1/\tau_{\text{eff}} - 1/\tau_{\text{Au}})$ versus Δn is of interest. However, a value for n_i needs to be decided for when converting the measured slope to J_{0e}, and this value should be stated when publicizing J_{0e} measurements. We use $n_i = 8.31\text{x}10^9$ cm^{-3} according to Ref. [7].

Our lateral determination of J_{0e} is based on photoconductance calibrated PL lifetime images [9]. PL images show the radiative recombination rate of the sample under illumination, i.e. the PL intensity I_{PL} can be expressed by [10]

$$I_{PL} \propto R_{rad} = B_{rad} np \approx B_{rad} \Delta n (N_{dop} + \Delta n), \tag{2}$$

and a calibration function $I_{\text{PL}}(a,C)$ [10]

$$I_{PL}(\Delta n) = a\Delta n + C\Delta n^2, \tag{3}$$

has to be found, where a and C are calibration constants, derived by comparing the area averaged PL intensity with the QSSPC signal over the coil at the same injection level, for several Δn values. For the calibration, a homogeneous part of the sample is used in order to reduce the uncertainty. The PL image is converted using (3) to an image of Δn, and τ_{eff} is then derived from

$$\tau_{eff} = \frac{\Delta n}{G}, \tag{4}$$

where G is the average carrier-generation rate per volume.

Two τ_{eff} images are taken under two distinct high-injection conditions. According to Eq. (1), the inverse lifetimes at each pixel of the two lifetime images are used, and J_{0e} is calculated according to:

$$J_{0e}(x,y) = \frac{qn_i^2 W}{2}\left[\frac{\left(1/\tau_{eff}(x,y) - 1/\tau_{Au}(x,y)\right)_{high}}{\Delta n_{high}(x,y) - \Delta n_{low}(x,y)} - \frac{\left(1/\tau_{eff}(x,y) - 1/\tau_{Au}(x,y)\right)_{low}}{\Delta n_{high}(x,y) - \Delta n_{low}(x,y)}\right]. \quad (5)$$

The factor ½ is due to the symmetrical sample preparation, where two identical emitters are diffused at the front and back surfaces of the sample.

Our calibrated lifetime images are derived using the LIS-R1 system from BT Imaging [11], which contains a Sinton Instruments photoconductance set-up [12]. The optics for the laser light allows for illumination levels of up to 10 suns. A schematic illustration of the set-up can be found for example in [9]. The optical reflectivity, required by the LIS-R1 system, is derived using a PerkinElmer UV/VIS spectrometer [13], while the wafer thickness is measured with a Käfer digital-dial gauge [14]. The emitter sheet resistance R_{sheet} is measured after phosphorus glass removal (PGR) using a four-point-probe setup.

3. Simulation method

As the measuring method has been developed only recently [3], we analyze the lateral behavior of J_{0e} by means of numerical device simulations in two dimensions. For this purpose, we use TCAD (Dessis) from Synopsys [15] to solve the fully coupled set of semiconductor equations, and we apply the physical models and parameters described in Ref. [16].

In device simulations, J_{0e} is not an input but a result from choosing a dopant profile, a surface recombination velocity S, and models such as Auger recombination, mobility etc. There are two main ways to extract J_{0e} from device simulations. One is to assume that all the current j that enters a dopant profile is caused to supply the recombination occurring within the dopant profile, i.e. j, p and n is probed at the base side of the space-charge region. Hence, there is

$$J_{0e} = \frac{j}{pn - n_i^2} n_i^2, \quad (6)$$

Please note that the local j is not accessible to experiment [17]. Thus we use a second simulation method, that reproduces Kane and Swansons's experiment [2], which means that the photo-generation density G is ramped while

$$\tau_{eff} = \frac{\Delta n}{R_{tot}} = \frac{\Delta n}{G} \quad (7)$$

is monitored, where $R_{tot} = R_{SRH}+R_{Au}+R_{rad}$, i.e. the sum of all recombination included in the simulation. The lateral derivation of J_{0e} in the simulation is done by averaging all values over an array with widths of 50 µm. No optical simulation is carried out of rays according to the spatial distribution of R_{rad}. This implies that all rays are detected where they are generated.

4. Sample preparation

To determine J_{0e}, wafers which are diffused and passivated identically on both sides, have a high resistivity ρ and a high τ_{eff}, are used, so that high-injection condition can be achieved. We use saw-damage etched p-type 6'' Cz material with a resistivity ρ = 6 – 12 Ωcm. The wafers receive a HF-dip followed by $POCl_3$ diffusion for forming a homogeneous n^+-region. To obtain a laser-doped selective emitter (LD-SE), the phosphorus glass is heated by a laser, leading to additional local phosphorous diffusion, and thus forming the n^{++} region. The processing is finished by applying phosphorus glass removal (PGR) and SiN deposition by PECVD on both sides of the wafers.

Two different test structures where produced, which are schematically shown in Fig. 1. The first has four square-shaped n^{++} regions with a size of 40 mm by 40 mm symmetrically on the front and back side. The second structure investigates the J_{0e} dependence on the laser intensity for the laser-doping process. For that, rectangular-shaped n^{++} regions with a size of 10 mm by 30 mm are produced on one wafer with different laser intensities, but just on one side. The latter sample is investigated before and after firing in a standard industrial belt furnace for screen printing. These structures were produced by laser-doping, where laser stripes were placed very close to each other, possibly with overlap due to positioning accuracy, causing double diffusions.

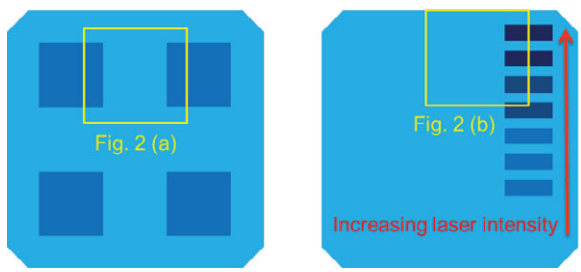

Fig. 1. Test structures: (a) symmetrical four square-shaped n^{++} regions with a size of 40 mm by 40 mm, (b) one-sided rectangular-shaped n^{++} regions with a size of 10 mm by 30 mm with different laser intensities.

5. Results

To calculate the experimental J_{0e} image, two calibrated lifetime images with a resolution of 403 pixels by 363 pixels are taken at approximately 4 and 8 suns. This corresponds to an injection level of about 4×10^{15} cm^{-3} and 8×10^{15} cm^{-3} in the n^+ region, denoted as "2" in Fig. 2 (a).

Also in Fig. 2 (a), two small parts of square-shaped n^{++} structures with a size of 40 mm by 40 mm are partly visible on the left and right edges of the image as bright areas. In the area "2" of Fig. 2 (a), an area-averaged J_{0e} of 238±15 fA/cm² is derived for the homogeneous n^+ emitter. For the area "1", it is 419±19 fA/cm², which is the n^{++} region. The uncertainty is the standard deviations of the area-average. We deliberately made the n^{++} regions larger than the coil of the QSSPC in order to directly compare a QSSPC measurement of a n^{++} region with the J_{0e} image. We observe a deviation in J_{0e} between the two measurement techniques that is smaller than 10% in relative terms.

Some artefacts are visible in Fig. 2 (a) and Fig. 3 (a). The round structures in the centre are due to the difference between the optical reflectivity of the QSSPC coil and the rest of the QSSPC stage. The brighter stripes at the edges of the images are due to effects in the optical system.

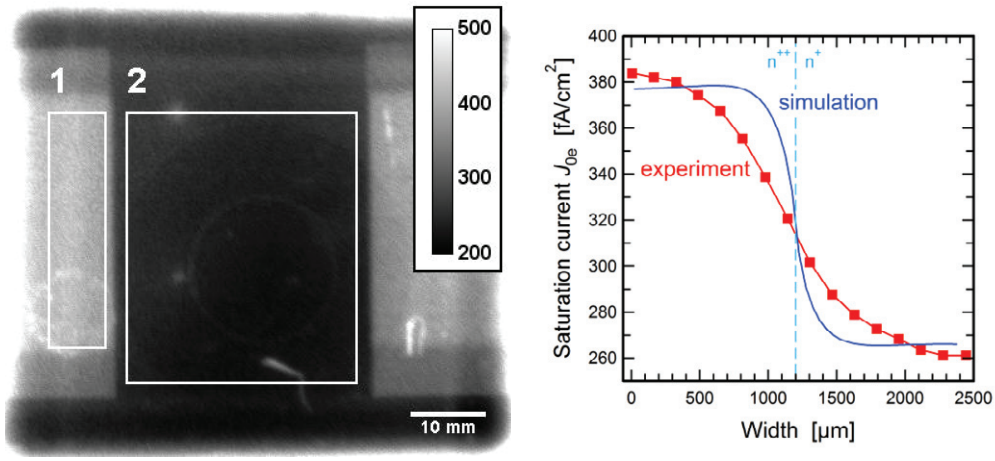

Fig. 2. (a) Emitter saturation current density image where two selective emitter structures on the left and right side are visible (J_{0e} in fA/cm²). The round structures are artefacts. (b) Comparison of experimental (from area "1" to "2") and simulated (τ_{eff} method) linescans of J_{0e}.

For validation of the derived J_{0e} image, we compare a linescan going from the area "1" to "2" in Fig. 2(a), with numerical simulations in Fig. 2(b). In experiment, a saturation of J_{0e} is achieved within 2 mm, while the simulation (τ_{eff} method) shows a saturation within 1mm under a generation rate of $G = 5\text{x}10^{19}$ cm^{-3} similar to the experiment. We assume that this is so because the detected rays are generated at various lateral positions due to different optical paths caused by reflection at the rear surface, sample stage and scattering at the front surface. The reason for the rather wide J_{0e} transition between the abrupt change from n^{++} to n^{+} is mainly due to lateral currents in the base, causing a blurring of the electron and hole density n and p in the base, which is measured by PL. We found that at G as high as $5\text{x}10^{20}$ cm^{-3}, the simulations show a lateral resolution of about 0.5 mm for the abrupt transition from n^{++} to n^{+}, which is due to the reduction of the diffusion length at higher injection levels.

By means of the J_{0e} imaging method, we analyze the J_{0e} dependence on laser-doping with different laser intensities. For that, J_{0e} of the rectangles of the second structure in Fig. 1 (b) are determined with the described method on a single wafer as exemplarily shown in Fig. 3 (a) for three rectangles. In Fig. 3 (b), the derived J_{0e} and the R_{sheet} for each square is shown depending on the relative laser intensity before and after firing the sample in a belt furnace. For increasing laser intensities the J_{0e} first increases up to a relative laser intensity of 42% and then decreases, while the R_{sheet} decreases from about 95 Ω/□ to 26 Ω/□. Qualitatively similar results can be found in [18], which confirms the applicability of the method. Note that the benefit of the increased SiN passivation quality due to firing in the belt furnace is higher for the homogeneous emitter than for the laser-doped emitters with a high R_{sheet}. E.g. the J_{0e} of the homogenous emitter drops from 234±14 fA/cm² to 83±7 fA/cm², while J_{0e} of the selective emitter of R_{sheet} = 26 Ω/□ drops from 240±13 fA/cm² to 136±6 fA/cm². The second structure is suitable for investigating the recombination activity of a laser-doped emitter, which can be used for the optimization of selective emitter solar cells. However, the influence of the metallization step is not considered, i.e. additionally introduced recombination and the contact resistance R_C of the contact formation are not taken account of.

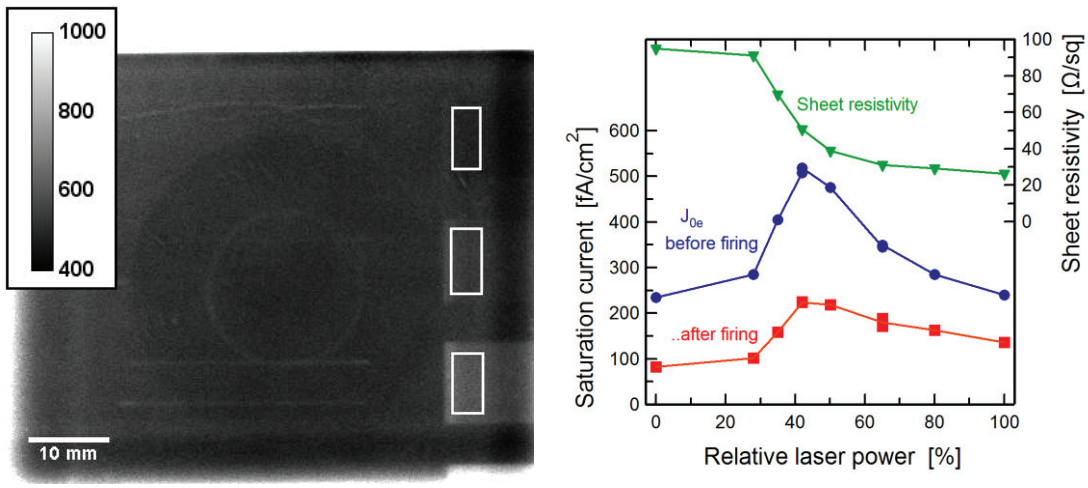

Fig. 3. (a) Example J_{0e} image of the second structure in fA/cm². (b) Dependence of J_{0e} and R_{sheet} on the relative laser intensity of the laser-doping process. J_{0e} is shown before/after firing in a belt furnace

6. Conclusions

The method of imaging J_{0e} is investigated experimentally and by numerical simulations. By comparison, a limited resolution of a feature size of an inhomogeneous emitter is determined to be theoretically between 0.5-1.0 mm and experimentally about 2 mm. It is found that the reason is the lateral current in the base blurring the charge carrier densities n and p, which are experimentally observed by PL measurements. The successful application of the method used to investigate the influence of laser power to squared selective emitter structures shows that the R_{sheet} decreases with increasing laser power, while the recombination activity of the emitter characterized by J_{0e} first increases and then decreases as expected.

Acknowledgements

This work was supported by the German Ministry for the Environment (BMU) under Contract No. 0325204 (project SIMPSONS). The authors would like to thank the characterization group at SolarWorld Innovations for their support.

References

[1]D. E. Kane and R. M. Swanson. Measurement of the emitter saturation current by a contactless photoconductivity method. Proc. *18th IEEE PV Specialists Conf.,1985*, pp. 578–581.

[2] R. A. Sinton and A. Cuevas. Contactless determination of current–voltage characteristics and minority carrier lifetimes in semiconductors from quasi-steady-state photoconductance data., *Appl. Phys. Lett.*, vol. 69, pp. 2510–2512, Oct. 1996.

[3] M. Müller, P. P. Altermatt, K. Schlegel, G. Fischer. A method for imaging the emitter saturation current with lateral resolution. Submitted to *IEEE Journal of Photovoltaics*.

[4] A. Cuevas. The effect of emitter recombination on the effective lifetime of silicon wafers. *Solar Energy Materials & Solar Cells*, vol. **57**, pp. 277-290, Aug. 1999.

[5] C. Reichel, F. Granek, J. Benick, O. Schultz-Wittmann, and S.W. Glunz. Comparison of emitter saturation current densities determined by injection-dependent lifetime spectroscopy in high and low injection regimes. Progr. in PV (2010, May), DOI: 10.1002/pip.942.

[6] M. J. Kerr and A. Cuevas. General parameterization of Auger recombination in crystalline silicon. *J. Appl. Phys.* vol. **91**, pp. 2473–2480, Feb. 2008.

[7] K. Misiakos and D. Tsamakis. Accurate measurements of the silicon intrinsic carrier density from 78 to 340 K. *J. Appl. Phys*. vol. **74**, pp. 3293–3297, Sep. 1993.

[8] P. P. Altermatt, A. Schenk, F. Geelhaar, and G. Heiser. Reassessment of the intrinsic carrier density in crystalline silicon in view of band-gap narrowing. *J. Appl. Phys.* vol. **93**, pp. 1598–1604, Feb 2003.

[9] S. Herlufsen, J. Schmidt, D. Hinken, K. Bothe, and R. Brendel. Photoconductance-calibrated photoluminescence lifetime imaging of crystalline silicon. *Phys. Stat. Sol. (RRL)*, vol. 2, 245–247, Sep. 2008.

[10] S. Herlufsen, J. Schmidt, D. Hinken, K. Bothe, and R. Brendel. Camera-based photoluminescence lifetime imaging of crystalline silicon wafers. *Proc. 24th EU PVSE Conf., 2AO.1.3, 2009*.

[11] BT Imaging, Sydney, Australia, http://www.btimaging.com/

[12] Sinton Consulting, Boulder, CO, http://www.sintoninstruments.com/

[13] PerkinElmer, Waltham , MA, http://www.perkinelmer.com/

[14] Käfer Messuhrenfabrik, Villingen-Schwenningen, Germany, http:// www.kaefer-messuhren.de/

[15] TCAD, Version 2011.09, Synopsys, Mountain View, CA, http://www.synopsys.com/

P. P. Altermatt. Models for numerical device simulations of crystalline silicon solar cells—a review. *J. Computational Electronics;* **vol. 10**, p. 314, 2011.

[16] H. Mäckel and K. Varner, On the determination of the emitter saturation current density from lifetime measurements of silicon devices, Progress in PV (2012), DOI: 10.1002/pip.2167.

[17] B. Paviet-Salomon, S. Gall, R. Monna, S. Manuel, A. Slaoui. Experimental and analytical study of saturation current density of laser-doped phosphorus emitters for silicon solar cells. **Solar Energy Materials & Solar Cells,** vol. 95, pp. 2536-2539, Mar. 2011.